Article

Silver Tungstate Obtained via Successive Seed Crystal Growth: Structural, Morphological, Optical, and Photocatalytic Properties

Germano P. Santos, [a,b] *Francisco C. M. Silva,*[c] *João F. Cruz-Filho,*[a,c]
Roberto A. S. Luz[a,c] *and Geraldo E. Luz Jr.* *,[a,c]

ªDepartamento de Química, Universidade Federal do Piauí, 64049-550 Teresina-PI, Brazil

ᵇInstituto Federal do Piauí, 64053-390 Teresina-PI, Brazil

*ᶜGrEEnTeC-CCN, Universidade Estadual do Piuaí, Rua João Cabral S/N,
64002-150 Teresina-PI, Brazil*

Synthesis routes and parameters such as synthesis time, precursor molar ratio, pH, and temperature are critical for generating oxides of various sizes and morphological aspects. However, there is no information on how to prepare silver tungstate (Ag_2WO_4) crystals of different shapes and sizes under laboratory conditions and without using sulfating agents. In this study, we attempted to fill this gap by preparing α-Ag_2WO_4 crystals of various sizes and morphologies using the coprecipitation method in a 3 h interval at room temperature and without using sulfating agents. The powder X-ray diffraction analysis confirmed that all crystals had an orthorhombic structure, whereas Fourier-transform infrared spectroscopy revealed the degree of structural disorder in the bonds between the atoms in the materials. Scanning electron microscopy revealed that the α-Ag_2WO_4 crystals had different sizes (5.37-26.83 μm) and morphologies (tetragonal prism, rod, and cypress leave-like rod), whereas ultraviolet-visible diffuse reflectance spectroscopy analysis indicated the optical band gap energy (2.92-3.05 eV), calculated using the method proposed by Kubelka and Munk. Catalytic tests revealed that the synthesized samples with the smallest crystals (AW1) and a tetragonal prism morphology degraded dye more efficiently (apparent rate constant (k) = 5.86×10^{-3} min^{-1}) than other samples.

Keywords: silver tungstate, degradation, semiconductor, coprecipitation method

Introduction

In recent years, researchers have been particularly interested in investigating the influence of morphological aspects on the structural, electrical, optical, physical, and chemical properties of materials.[1-10] Although it is challenging to modify and study the morphology of materials, the benefits are evident, such as the ability to understand the interrelationship between differences in morphology and catalytic reactions.

Several studies[11-16] have investigated the influence of morphological aspects on the photocatalytic properties and structure of semiconductor materials in the last decade. Silver tungstate (Ag_2WO_4) stands out among these compounds because of its crystalline structure, which includes an alpha (α) phase with an orthorhombic type,

a beta (β) phase with a hexagonal type, and a gamma (γ) phase with a cubic type.[8,17] Additionally, α-Ag_2WO_4 is in the most thermodynamically stable phase and has a promising application as a photocatalyst.[18,19] The scientific community devotes particular attention to α-Ag_2WO_4 because it has a wide range of applications in different fields, such as photoluminescence[20] and sensors.[21]

Some of the main advantages of this inorganic semiconductor are that it is easy to obtain via different conventional synthetic methods[11,12] and that its crystal morphology and size, which are two critical parameters for investigating photocatalytic activity and dye degradation, can be controlled.[6] In this case, the conditions and parameters for the type of synthesis are critical for obtaining the desired crystal size and morphology.[13]

There are only few research reports on the morphology of α-Ag_2WO_4 photocatalysts. Cavalcante *et al*.[14] proposed the first investigation into the morphologies of α-Ag_2WO_4 crystals in 2012. They demonstrated a new methodology

for improving the photocatalytic performance of semiconductors. The investigation aimed to find a relationship between photocatalytic activity and the faces of the compound's ridges.

Longo and co-workers[15] demonstrated that the morphology and mechanisms of α-Ag_2WO_4 crystal formation can be controlled by adjusting the synthesis time, precursor molar ratio, pH, and temperature. In addition, they investigated the electronic, structural, and energetic properties of α-Ag_2WO_4 crystals using experimental data and theoretical calculations.

Recent studies have demonstrated the effect of temperature on the morphology of α-Ag_2WO_4 crystals during synthesis. In a previous study,[16] rods of various sizes and morphologies were obtained by varying the average temperature of the reaction.

However, to the best of our knowledge, the preparation and investigation of the structural, morphological, optical, and photocatalytic properties of α-Ag_2WO_4 crystals produced by successive seed crystal growth in the absence of surfactants have not been reported yet. Surfactants are generally used because of their influence on crystal morphology and growth.[22,23] The morphology of a synthesized material is of paramount importance in view of its effects on the physical and chemical properties, structure, and size of crystals obtained.[24,25]

In this regard, we present a facile approach for producing morphologically distinct α-Ag_2WO_4 crystals. In addition, the morphology and structural properties of the crystals were studied. Most importantly, the effect of size and morphology on the photocatalytic activity of α-Ag_2WO_4 crystals for Rhodamine B (RhB) was investigated.

Experimental

Reagents

Silver nitrate ($AgNO_3$) (99.995%, Sigma-Aldrich, St. Louis, USA), sodium tungstate ($Na_2WO_4 \cdot 2H_2O$) (99.995%, Sigma-Aldrich, St. Louis, USA), and distilled water were used in all synthesis procedures. All the reagents were analytical grade and were used without further purification.

Synthesis of α-Ag_2WO_4 crystals

The α-Ag_2WO_4 crystals were synthesized using the coprecipitation method.[18,23,26] For the synthesis, 100 mL of a Na_2WO_4 solution (0.01 mol L^{-1}) were added slowly into 100 mL of $AgNO_3$ solution (0.02 mol L^{-1}). Under vigorous stirring (ca. 30 rpm) at 25 °C for 3 h, the above mixture

formed a yellow suspension instantly and then formed a white precipitate after a few minutes. The α-Ag_2WO_4 crystals in suspension were separated by decanting (10 min), washed with deionized water (ca. 15 times), and then dried at 65 °C for 10 h before being denoted as AW1, as shown in Figure 1.

New crystals (AW2, AW3, AW4, AW5, and AW6) with different morphologies were produced in a similar manner as the AW1 crystals, except that 10 mg of AWX (X represents crystals obtained in the synthesis prior to new crystal formation) was added to the $AgNO_3$ solution. Thus, 10 mg of AW1 was added to the $AgNO_3$ solution to produce AW2, and 10 mg of AW2 was added to produce AW3, and so on. During the synthesis procedure, no sulfating agent was used to control the crystal growth for obtaining crystals of desired shapes and sizes.

α-Ag_2WO_4 crystals characterizations

The α-Ag_2WO_4 crystals were structurally characterized using powder X-ray diffraction (XRD), Fourier-transform infrared (FTIR) spectroscopy, Raman spectroscopy, scanning electron microscopy (SEM) and ultraviolet-visible (UV-Vis) diffuse reflectance, all of which were previously described in the literature.[27]

XRD patterns

The α-Ag_2WO_4 crystals were characterized by XRD using an XRD-6000 diffractometer (Shimadzu, Japan), scanning from 5 to 120° at a speed of 1° min^{-1}, with a step of 0.02° and Cu Kα radiation (1.5418 Å).

FTIR spectroscopy

Fourier transform infrared (FTIR) analyses were performed using a PerkinElmer Spectrum 100 GX FTIR system set to measure 16 cumulative scans at 4 cm^{-1} in a range of 400-1100 cm^{-1} using the dilution method on potassium bromide (KBr) pellets.[27]

Raman spectroscopy analysis

Raman vibrational spectra were collected using a SENTERRA spectrometer (Bruker, Germany), which was attached to a charge-coupled device detector system. Data were collected in the range of 50-1000 cm^{-1} with an integration time of 10 s^{-1} using an excitation laser with a wavelength of 532 nm, a maximum power of 0.20 mW, and a resolution of 4 cm^{-1}.[22,28]

SEM analysis

The morphologies, shapes and sizes of the α-Ag_2WO_4 crystals were investigated using a SEM equipped with
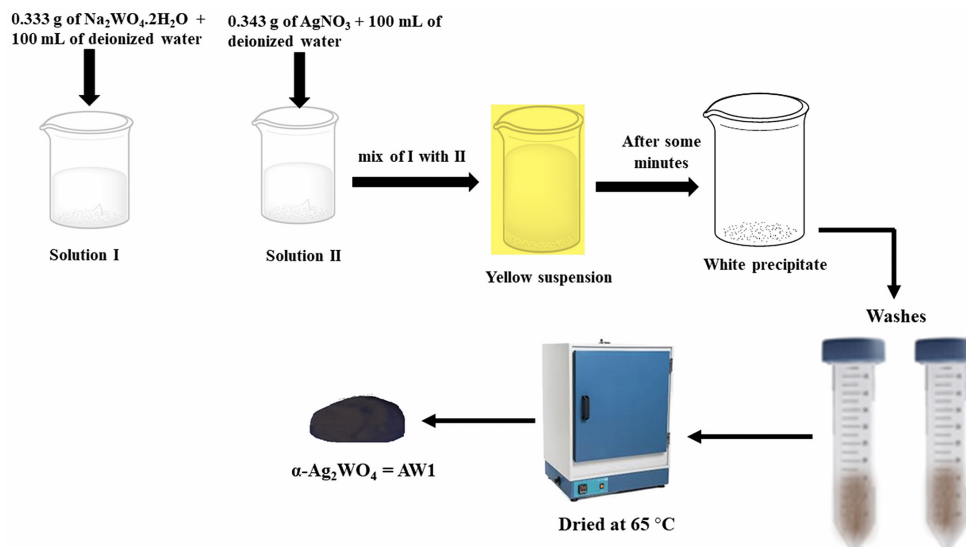
Figure 1. Scheme of synthesis of α-Ag$_2$WO$_4$ by coprecipitation method at 25 °C for 3 h.

FEI COMPANY (Netherlands), Model Quanta FEG 250 operated at 20 kV.[18]

Ultraviolet-visible (UV-Vis) diffuse reflectance

For the study and optical characterization, the band gap values were estimated using the UV-Vis diffuse reflectance data, an integrating sphere for solid analysis, and barium sulfate (BaSO$_4$, ≥ 99.9%, Sigma-Aldrich, St. Louis, USA) as the reflectance standard. The spectra were collected in the range of 200-900 nm at a scanning speed of 1 nm s^{-1} in a Shimadzu model UV-2600 spectrophotometer (Shimadzu, Japan).

The band gap (E$_g$) of the α-Ag$_2$WO$_4$ powders was estimated by conducting spectroscopy in the UV-Vis region using the Wood and Tauc function[29] in the reflectance data obtained using the Kubelka-Munk equation.[12] The E$_g$ of the samples was determined by fitting the absorption data to the direct transition equation αhν = A(hν − E$_g$)$^{1/2}$, where α is the absorption coefficient, hν is the photon energy, A is a proportionality constant, and E$_g$ is the optical band gap. This was achieved by plotting (αhν)^2 as a function of photon energy and extrapolating the linear portion of the curve to absorption equal to zero.[3,16,30]

Photocatalytic tests

The photocatalytic efficiency of the synthesized α-Ag$_2$WO$_4$ crystals was studied by performing photodegradation tests in an aqueous RhB dye solution using methodologies previously described in the literature.[14,16]

To perform the photocatalysis experiments, 0.05 g of the α-Ag$_2$WO$_4$ powders from each sample was stirred with 50 mL of the aqueous dye solution (10^{-5} mol L^{-1}).

Thereafter, each mixture was kept in the dark for 30 min to achieve adsorption/desorption equilibrium. Separately, the suspensions were kept under constant stirring and irradiated in a photoreactor with six lamps (Philips TL-D, 15 W; λ = 254 nm), and the temperature was maintained at 20 °C using a thermostatic bath.

The solutions were monitored by extracting 5.0 mL aliquots of the solution at 15 min intervals, centrifuging them at 4500 rpm for 5 min to separate the solid catalyst from the liquid phase, and discarding the precipitate. The data were collected using a quartz cuvette in the spectral range of 200-800 nm to evaluate the characteristic RhB absorbance value (λ$_{max}$ = 554 nm) in a Shimadzu model UV-2600 spectrophotometer (Shimadzu, Japan).[27-32]

Results and Discussion

XRD patterns

The crystal phase and crystallinity of the obtained Ag$_2$WO$_4$ samples were confirmed by XRD. Figure 2 shows the XRD patterns of the AW1, AW2, AW3, AW4, AW5, and AW6 samples. The diffraction pattern profiles for α-Ag$_2$WO$_4$ are noticeable in the XRD patterns because the reflection peaks are intense and sharp. The materials were found to have an orthorhombic structure and a P*n2n* space group, with octahedral clusters [WO$_6$] and [AgOn]: n = 7, deltahedral [AgO$_7$]; n = 6, octahedral [AgO$_6$]; n = 4, tetrahedral [AgO$_4$]; n = 2, angular [AgO$_2$].[15,29,30]

As shown in Figure 2a, the diffraction peaks at 10.95, 14.54, 15.87, 18.40, 26.07, 29.08, 30.04, 32.26, 32.72, 34.17, 44.71, 48.97, 53.03, 55.54, 56.13, 57.53, and 59.17° in the range of 2θ = 10-90° are attributed to the (110), (020),

(011), (101), (310), (311), (002), (231), (400), (141), (402), (512), (303), (352), (313), (460), and (413) crystal planes of α-Ag$_2$WO$_4$, respectively. Despite the displacement effect of diffraction peaks related to the effect of orientation preference, suggestively attributed to the morphology of the sample, the peaks can be correlated with the data in the Inorganic Crystal Structure Database (ICSD) 4165 and the literature.[22,30]

Variations in the intensity of the diffraction peaks located at 29.08, 30.04, 32.26, and 32.72° can be observed in Figure 2b. The orthorhombic α-Ag$_2$WO$_4$ peaks located at 30.04° (002) and 32.72° (400) are relatively weak for the AW1, AW3, and AW5 samples, whereas these peaks are relatively intense for the AW2, AW4, and AW6 samples. However, the peaks located at 29.08° (311) and 32.26° (231) are relatively weak for the AW2, AW4, and AW6 samples, whereas these peaks are relatively intense for the AW1, AW3, and AW5 samples.

According to the literature, differences in peak intensity in diffractograms indicate that samples contain crystals with various morphologies[27] and sizes,[19,33] which could be related to microextension anisotropic and preferential effects of the organization of the ions in the structure of the material.[2,34,35]

In addition, the formation process is responsible for the differences in α-Ag$_2$WO$_4$ crystals. During the precipitation or nucleation process, these crystals can grow from seeds (nanocrystals)[36,37] via ionic attraction (between Ag$^+$ and WO$_4^{2-}$), resulting in the formation of nanocrystals with a coalescence process, followed by compaction, and then the formation of different microcrystals, as commonly observed when producing α-Ag$_2$WO$_4$ crystals using the precipitation method.[14,15,18,36-40]

Therefore, the synthesis procedure used to obtain the AW1, AW2, AW3, AW4, AW5, and AW6 samples is believed to be efficient because different α-Ag$_2$WO$_4$ crystals were formed from the synthesis sequence, which was always from the previous synthesis.
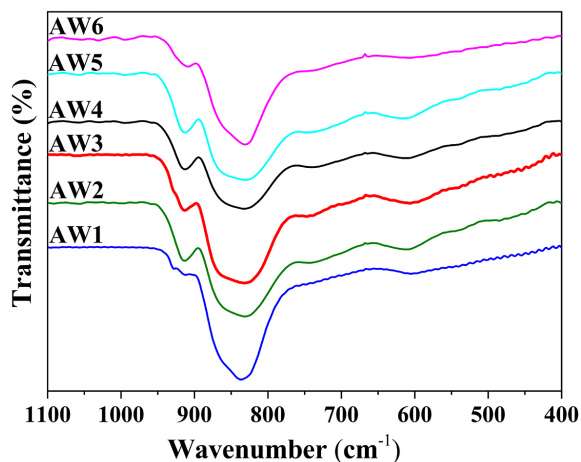
FTIR spectroscopy

Infrared spectroscopy was used as a tool to extract information from the α-Ag$_2$WO$_4$ crystals, including the degree of order/structural disorder of the bonds between the atoms in the synthesized crystals prepared using the coprecipitation method.

Figure 3 shows the spectra of the α-Ag$_2$WO$_4$ crystals. All the IR-active modes of the α-Ag$_2$WO$_4$ crystals are related to an orthorhombic structure, which is consistent with previous findings.[12,27,31] The spectra of powder materials are known to be strongly influenced by a wide variety of parameters such as crystal size and shape.[1-3,40]

The FTIR spectra (Figure 3) reveal two intense absorption bands at 834 and 915 cm^{-1} for all the α-Ag$_2$WO$_4$ crystals. The absorption band at 834 cm^{-1}, which is attributed to the bonds between ($\leftarrow$O$\leftarrow$W$\leftarrow$O$\leftarrow$)/($\rightarrow$O$\rightarrow$W$\rightarrow$O$\rightarrow$) of the antisymmetric stretching vibrations within the distorted [WO$_6$] clusters,[14,23] is less intense for the AW1 sample, and this may be due to the increased interaction forces between the W–O bonds or distortions in the [WO$_6$] clusters in the network for the small analyzed crystals (5.40 μm).[14] Conversely, the band observed at around 640 cm^{-1}, which can be attributed to the bridging oxygen atoms in the W$_2$O$_2$ asymmetric stretching mode,[41] is less intense for the AW6
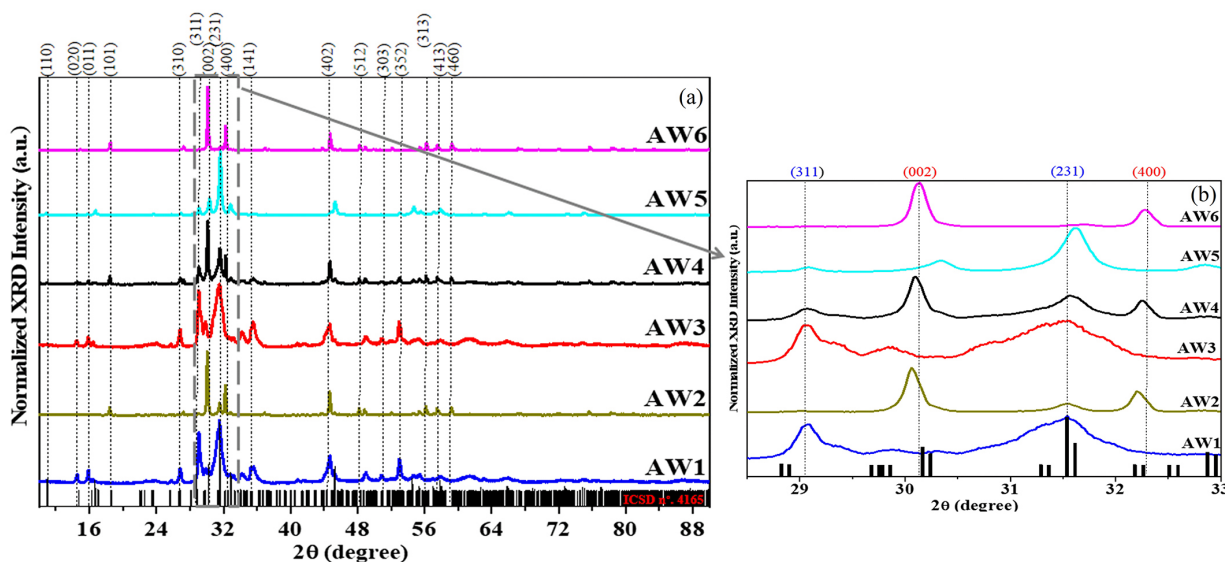
Figure 2. (a) X-ray diffraction patterns for the AW1, AW2, AW3, AW4, AW5 and AW6 samples prepared by the coprecipitation method at 25 °C for 3 h. The vertical lines indicate the peak position in the direction of each plane. (b) Enlarged view of the diffracted region between 28 and 33°.

Figure 3. FTIR (KBr) spectra for the AW1, AW2, AW3, AW4, AW5 and AW6 samples prepared by the coprecipitation method at 25 ºC for 3 h.

Raman spectroscopy analysis

Raman spectroscopy was used to obtain structural information on the synthesized samples. This tool is feasible for obtaining the structural information of metal oxides.[31]

Figure 4 shows the Raman spectra of the AW1, AW2, AW3, AW4, AW5, and AW6 samples. Sixteen active modes of the 23 modes predicted for the orthorhombic structure (i.e., the alpha-phase α-Ag$_2$WO$_4$) associated with the punctual group of symmetry C_{2v}^{10} were observed in all the spectra.[42-44] This may be because some modes had very low intensity signals and because of equipment limitations.

The active modes between 1000 and 500 cm^{-1} are related to the vibrations in the [WO$_6$] clusters, while the active modes between 500 and 60 cm^{-1} are associated with the movements of silver ions present in the [AgO$_7$], [AgO$_6$], [AgO$_4$], and [AgO$_2$] clusters.[23] Thus, modes positioned at 898 (A$_{1g}$), 876 (A$_{1g}$), 809 (A$_{2g}$), 770 (A$_{1g}$), 728 (B$_{2g}$), 648 (B$_{1g}$), and 505 cm^{-1} (B$_{2g}$) are related to the symmetrical stretches of the ($\leftarrow$O–W–O/O–W–O$\rightarrow$) bonds present in the [WO$_6$] clusters of the octahedral symmetry.[27,30,31,45,46]

In particular, the out-of-plane bending modes of W–O–O–W were observed at 300 cm^{-1} (A$_{2g}$). The mode at 648 cm^{-1} is related to the stretching vibration of W–O–O–W. The modes located at 728 and 770 cm^{-1} are due to the symmetrical stretching of the W–O–O–W and W–O bonds. The mode centered on 809 cm^{-1} is related to the antisymmetric stretching of W–O–W and W–O, and the mode at 876 cm^{-1} (A$_{1g}$) is related to the symmetric stretching of the O–W–O bonds in the [WO$_6$] octahedral.[46,47] The data shown in Figure 4 indicate that
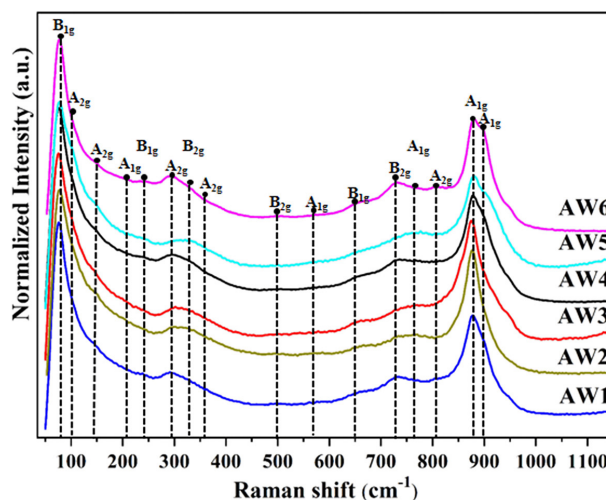
Figure 4. Raman spectra of AW1, AW2, AW3, AW4, AW5 and AW6 samples synthesized by coprecipitation method at 25 ºC for 3 h. The vertical lines indicate the peak position of active modes.

the α-Ag$_2$WO$_4$ structure is similar to that reported in the literature.[20,30,45,47-49]

SEM analysis

The physical and chemical properties of α-Ag$_2$WO$_4$ depend on the size, shape, composition, structure, and surface chemistry of the crystals. The SEM images were vital for understanding these properties, the morphological information, and the growth process of the α-Ag$_2$WO$_4$ crystals obtained using the synthetic route presented herein.

Figure 5a shows the SEM images of the α-Ag$_2$WO$_4$ materials, in which crystals of different sizes and morphologies can be observed. These morphological aspects observed in α-Ag$_2$WO$_4$ crystals are due to the synthetic method used, which consists of a strategy of successive crystal growth. The efficiency of the method was confirmed by means of a duplicate experiment (S1) for samples AW1 and AW2. The average crystals sizes analysis was conducted using SEM images for the samples, calculated from the randomly selected 150 crystals in each sample using an image analysis software (ImageJ).[29,50] The histograms (Figure S2, Supplementary Information (SI) section) obtained from of SEM images (Figure 5a) showed average width of 1.50 μm and average length between 5.37 and 26.83 μm for the α-Ag$_2$WO$_4$ crystals. The estimation of the size of the particles presented in the histograms does not follow the limits of applicability of the Scherrer equation. According to the literature,[51-53] the Scherrer equation is valid only for crystallite sizes up to a few hundred nanometers (ca. 200 nm).

Table 1 contains information on the morphology, average length (μm), and average thickness (μm) of the

Table 1. Type of morphologies, average length and average thickness of the α-Ag$_2$WO$_4$ crystals obtained by coprecipitation method at 25 ºC for 3 h

Sample	Morphology	Average length / μm	Average thickness / μm
AW1	tetragonal prism	5.40	1.45
AW2	rod-like	9.40	1.41
AW3	rod-like	13.10	1.65
AW4	rod-like	3.0	2.62
AW5	cypress leave-liked	26.80	2.38
AW6	rod-like	9.50	1.10

α-Ag$_2$WO$_4$ crystals obtained from the analysis of the SEM micrographs of the samples.

As shown in Figure 5a, three different morphologies were observed in the synthesized crystals: tetragonal prism for the AW1 crystals; rod-like morphology for the AW2, AW3, AW4, and AW6 crystals; and regular cypress leave-like morphology for the AW5 crystals.

In addition, nanocrystals were observed on the microcrystals in the AW4, AW5, and AW6 samples. This could be related to the uncontrolled formation of nanocrystals, which acted as seeds for the formation of the microcrystals since no crystal growth control agent was used during the synthesis procedure.[54,55] Thus, slow and heterogeneous nanocrystal nucleation occurs first, followed by the formation of large and polydisperse products.[56-58]
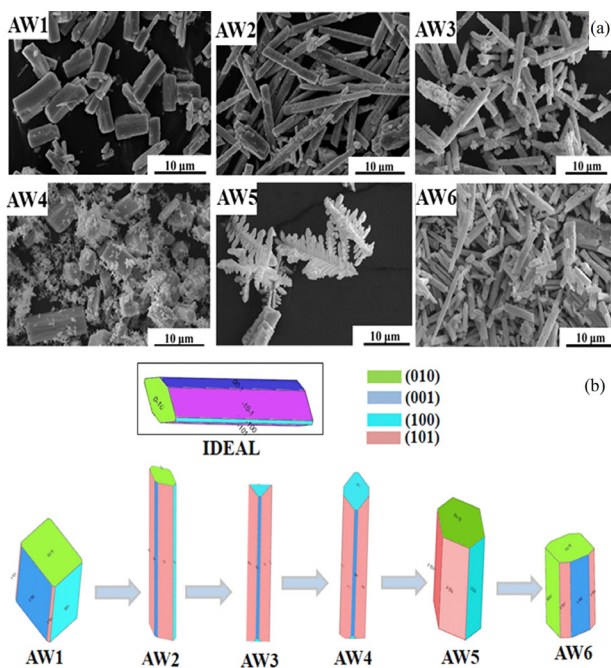
Figure 5. (a) SEM images for the AW1, AW2, AW3, AW4, AW5 and AW6 samples processed by the coprecipitation method at 25 ºC for 3 h. (b) Illustrative scheme for the α-Ag$_2$WO$_4$ crystal with the crystallographic planes (010), (001), (100) and (101).

The main factors that can cause a variation in the morphology of the α-Ag$_2$WO$_4$ crystals are synthesis procedure, surface energy, atomic distribution, agglomerated metals, and vacancies present on the surface of the crystals.[19,27,33,59,60]

Thus, theoretical investigations based on the experimental SEM and XRD data were critical for understanding the formation and growth of α-Ag$_2$WO$_4$ crystals produced via successive seed crystal growth. In this case, the crystal morphology editor/viewer KrystalShaper software (version 1.3.1 for Windows)[15,61] was used to determine the different types of morphologies for the crystals as well as the influence of the crystal plane on the morphology.

Based on the micrographs obtained by SEM and correlated with the relative intensities of the XRD diffractograms, the relative distance between the crystal faces and morphology can be obtained with its predominant faces (Figure 5b). The theoretical crystals were inserted into an orthorhombic cell and based on the data entered (relative distance between the faces), a growth preference in relation to the *b* axis can be observed (Figure S3, SI section), which agrees well with the micrographs obtained (Figure 5a).

Recent studies have reported that α-Ag$_2$WO$_4$ crystals can be obtained with different morphologies,[8,28] such as hexagonal rod-like and cuboid-like morphologies.[22] According to a previous study,[32] the growth of these crystals is related to the surface energy of the facets that constitute each microcrystalline morphology.

Previous studies[15,16,19,21] have shown that the morphological stability of α-Ag$_2$WO$_4$ crystals can be determined by the surface energies of the faces using a combination of experimental and theoretical approaches. In this regard, the morphology type is predicted by the relative stabilities of all the surfaces, with the lowest surface energy being preferred thermodynamically.[22] The surface energy values of α-Ag$_2$WO$_4$ crystals exhibit the following order of stability (010) < (100) < (001) < (110) < (101) < (011).[15,22]

In this manner, preferential growth occurs in the direction of the lowest energy plane (111) in crystals with rod-like morphologies.[37] Crystals with cubic morphology have a combination of facets with preferential growth toward the (010), (100), and (001) planes.[22,62]

However, according to the XRD (Figure 2a) and SEM (Figure 5a) data for the α-Ag$_2$WO$_4$ samples, the crystals had different morphologies after the synthesis sequence. The α-Ag$_2$WO$_4$ crystals in the AW1 sample favored the formation of microstructured cubes (Figure 5b) because of their preferential growth toward the (100) crystalline plane (Figure 6).[62]
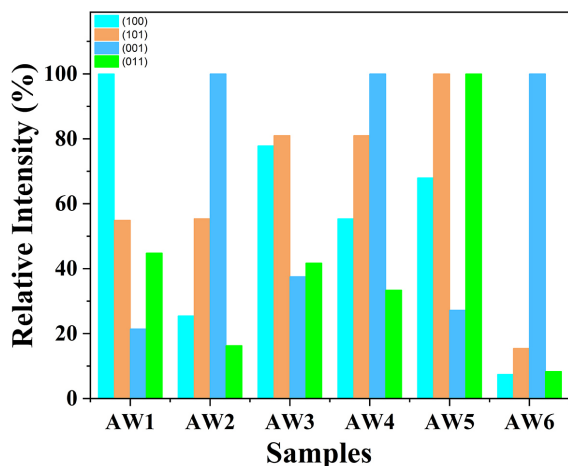
Figure 6. Graph of intensities relative to the (011), (001), (101) and (100) plans for AW1, AW2, AW3, AW4, AW5 and AW6 samples processed by the coprecipitation method at 25 ºC for 3 h.

The crystals from the AW2, AW4, and AW6 samples had a high degree of crystallinity, which can be indexed with the (002) and (440) planes, indicating that the α-Ag$_2$WO$_4$ crystal is a single crystal that grows in the (001) direction, favoring the formation of a ball-and-stick structure with rod-like morphology, which is a characteristic of the α-Ag$_2$WO$_4$ phase.[59,62] The crystals from the AW5 samples preferentially grew toward the (011) and (101) crystalline planes, favoring the formation of hexagonal-faced rods and regular leave-like cypress morphology. The formation of a well-defined surface morphology via particle growth has already been reported in the literature.[16,44,63]

This suggests that the morphological aspects of crystals are directly related to the synthesis procedure. Although there have been several studies on α-Ag$_2$WO$_4$ crystals with different morphologies,[3,15,16,26,39] this is the first study to obtain α-Ag$_2$WO$_4$ crystals of various morphologies via successive seed crystal growth using the coprecipitation method under laboratory conditions and without surfactant.

UV-Vis diffuse reflectance spectroscopy

The optical properties of the α-Ag$_2$WO$_4$ crystals were studied using UV-Vis diffuse reflectance spectroscopy, and the results are shown in Figure 7. The curves show absorption in a broad band at around 380-400 nm for all the α-Ag$_2$WO$_4$ samples. Figure 7 (inset) shows the estimated optical band gap values for each sample, which vary between 2.92 and 3.05 eV.

The variations in the band gap value of the material can be related to the synthesis method used and the crystal morphology, as previously reported.[20,42] The Ag$_2$WO$_4$ crystal is composed of several distinct clusters, with weak interactions between the O–W and O–Ag bonds, and the relative positions of the atoms (W, O, and Ag) vary in the constructed α-Ag$_2$WO$_4$ clusters.[43,60,62]

Although the differences in the E_g value are small, they can be related to the individual band intervals of each surface because the E_g is due to contributions from bond lengths and bond angles, which cause a redistribution of the electronic density and structure of the energy band.[31,44]
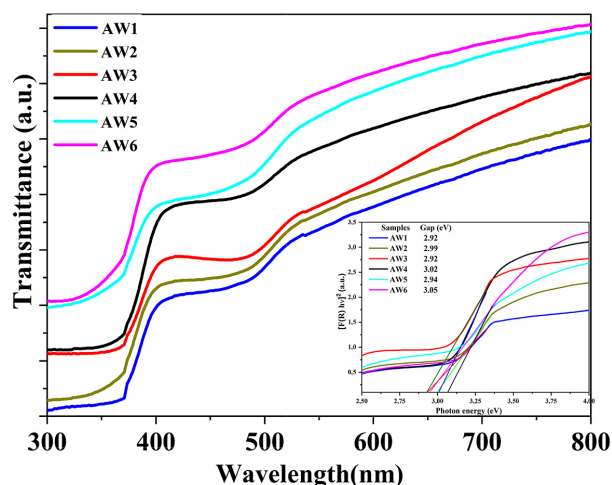

Figure 7. UV-Vis spectra of AW1, AW2, AW3, AW4, AW5 and AW6 and the inset shows direct band gap spectra obtained using the Kubelka-Munk method of the samples.

Photocatalytic activity for RhB dye degradation

Catalytic tests were conducted on the synthesized samples to study the degradation of the RhB dye molecules. These tests were conducted using previously published methodologies.[15,27] The photocatalytic activity of the powders was estimated using an RhB solution with a concentration of 10^{-5} mol L^{-1}.

Figure 8 shows the monitored spectra for the RhB dye solutions against photocatalytic tests in the absence and presence of the AW1, AW2, AW3, AW4, AW5, and AW6 samples. Before performing the tests in the presence of light, the mixture was agitated (200 rpm at 25 °C) in the dark in a catalytic cell coupled to a thermostatic bath until equilibrium was reached. Thereafter, aliquots were collected, and the absorbance was monitored at a wavelength of 554 nm, which is indicative of RhB.

RhB adsorption on the tested materials was negligible. This is consistent with the fact that the adsorption of RhB on α-Ag$_2$WO$_4$ is significant only when the pH of the solution is adjusted to 3.7.[27] Furthermore, several studies[3,14,18,26,60] have shown that several factors, such as structural defects, crystallographic orientation, electronic levels, surface energy, roughness, active surface area, facets, and
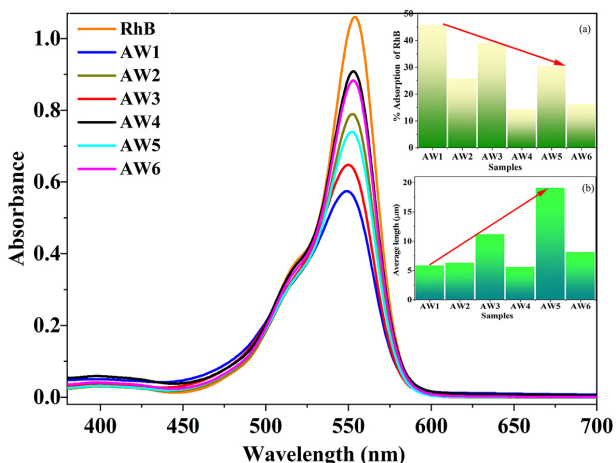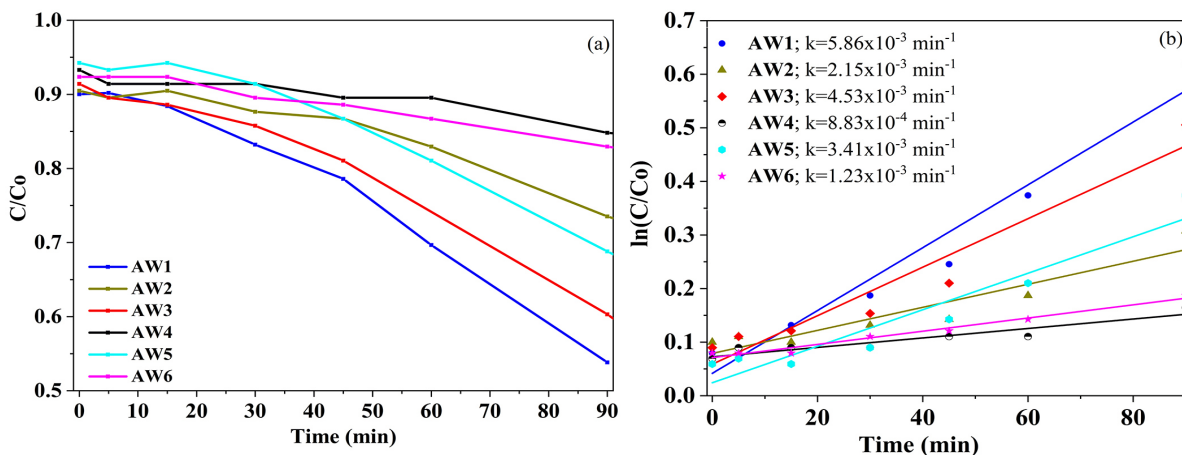
Figure 8. Photocatalytic tests on degradation of RhB dye in the presence AW1, AW2, AW3, AW4, AW5 and AW6 samples, using 50 mg of catalyst for 50 mL of solution of the dye, after 90 min of reaction. Insert (a) graph indicating the photocatalytic efficiency for the samples. (b) Graph indicating the average length of the crystals in the samples.

morphology of crystals, can influence the photocatalytic degradation of dyes for catalysts.

The photocatalytic activity of the α-Ag$_2$WO$_4$ crystals for the degradation of RhB dye in an aqueous solution under light irradiation was investigated in this study. The data in Figure 8 suggest that the different morphologies of the α-Ag$_2$WO$_4$ crystals caused differences in the degradation efficiency of the RhB dye. The results revealed distinct differences between the products, indicating that the morphology of the α-Ag$_2$WO$_4$ crystals had an effect on the degradation of the RhB dye (see the inset, Figure 8a).

Photocatalytic degradation of dyes by α-Ag$_2$WO$_4$ crystal catalysts can be explained using the exponential decay curve obtained from the relationship between the initial concentration (Co) and final concentration (C) of the dye solution after simulated solar irradiation, where Co and C are the RhB concentrations in the solution at times 0 and t, respectively.

As shown in Figure 8a, the maximum absorbance (at 554 nm) of the RhB solution decreased by 45, 40, and 30% after 90 min of reaction in the presence of the AW1, AW3, and AW5 samples as catalysts, respectively.

These results may be related to the formation of crystals in these samples. In addition, the crystal size estimated based on the SEM micrographs of these samples indicate that the small crystals (AW1), which had an average length of 5.40 µm, had the best photocatalytic performance, followed by the AW3 sample crystals, which had an average length of 9.40 µm, and then the AW5 crystals, which had an average length of 26.80 µm (see the inset, Figure 8b). Furthermore, the AW1, AW3, and AW5 samples were discovered to have a high degree of crystallinity, which can be indexed with the (231) plane (Figure 2b). Thus, crystals with improved crystallinity in the plane in the (231) direction have relatively low photocatalytic performance as their size increases.

The AW2 (25%), AW4 (14%), and AW6 (16%) samples had low photocatalytic degradation efficiencies. The crystals from these samples had preferential growth in the plane in the (001) direction (Figure 6). This suggests that crystals with preferential growth in this plane do not have good efficiency for photocatalytic degradation of RhB dyes.

According to the literature,[8,15,26] the photocatalytic performance of crystals is dependent on the facet that is exposed to the degradation of the RhB dye. The synthesis method used in this study favored the formation of crystals with different sizes and a high degree of crystallinity, which can be indexed with the (231) plane, and crystals of different morphologies with preferential growth in the direction of the (001) plane.

Figure 9 shows the corresponding pseudo-first-order kinetic plots and the apparent rate constant (k). The α-Ag$_2$WO$_4$ crystals in the AW1, AW2, and AW3 samples had degradation rates of 5.86×10^{-3}, 2.15×10^{-3}, and 4.53×10^{-3} min^{-1}, respectively, while those in the AW4 sample

Figure 9. (a) Photocatalytic degradation of RhB for the AW1, AW2, AW3, AW4, AW5 and AW6 samples and (b) corresponding plot of ln (C$_o$/C) *versus* time.

had a low degradation rate of 8.83×10^{-4} min^{-1}. The AW5 sample crystals, which had a regular cypress leaf-like shape, had a degradation rate of 3.41×10^{-3} min^{-1}, while the AW6 sample crystals had a degradation rate of 1.23×10^{-3} min^{-1}.

The photocatalytic performance of the AW1, AW2, AW3, AW4, AW5, and AW6 samples indicate that the morphology, size, and exposed facet of α-Ag$_2$WO$_4$ crystals have a significant effect on RhB degradation. These findings support previous findings.[15,22,26,30,62]

Conclusions

A new synthetic route using the coprecipitation method was successfully developed for producing α-Ag$_2$WO$_4$ crystals of different sizes and morphologies without the formation of secondary phases. Optical and structural characterization demonstrated that the synthesized α-Ag$_2$WO$_4$ crystals meet the requirements for the photocatalytic degradation of RhB dyes. Among the α-Ag$_2$WO$_4$ crystals, the rod-like crystal (average size of 5.37 μm) had the best photocatalytic performance for RhB dye degradation, with a degradation rate of 5.86×10^{-3} min^{-1}. Thus, it is suggested that the photocatalytic activity of α-Ag$_2$WO$_4$ crystals for RhB degradation is directly related to their size and morphology. Therefore, we present a promising approach for developing new photocatalysts for dye degradation.

Supplementary Information

Supplementary information (SEM images for the AW1 and AW2 samples, a duplicate experiment to confirm the control of the synthesis method, histograms showing the estimated average length, SEM and width distribution of α-Ag$_2$WO$_4$ microcrystals for AW1, AW2, AW3, AW4, AW5 and AW6 samples and schematic illustration of the crystals morphology based in the micrographs obtained by SEM and correlated with the relative intensities of the XRD diffractograms) are available free of charge at http://jbcs.sbq.org.br as PDF file.

Acknowledgments

References

1. Huang, Y. J.; Qi, G. R.; Chen, L. S.; *Appl. Catal., A* **2003**, *240*, 263. [Crossref]

2. Li, Y.; Shen, W.; *Chem. Soc. Rev.* **2014**, *43*, 1543. [Crossref]

3. Pereira, W. S.; Gozzo, C. B.; Longo, E.; Leite, E. R.; Sczancoski, J. C.; *Mater. Lett.* **2019**, *248*, 193. [Crossref]

4. Leal, G.; Cazalini, E. M.; Costa, D. S.; Cardoso, G. W. A.; Motta Jr., J. A.; Gomes, M. L. M.; Messmer, N. R.; Brazil, T. R.; Giacomelli, V. J.; Rezende, M. C.; *Mater. Res. Express* **2018**, *5*, 105603. [Crossref]

5. Carbone, M.; Bauer, E. M.; Micheli, L.; Missori, M.; *Colloids Surf., A* **2017**, *532*, 178. [Crossref]

6. He, H.; Xue, S.; Wu, Z.; Yu, C.; Yang, K.; Zhu, L.; Zhou, W.; Liu, R.; *J. Mater. Res.* **2016**, *31*, 2598. [Crossref]

7. Lisitsyn, V. M.; Valiev, D. T.; Tupitsyna, I. A.; Polisadova, E. F.; Oleshko, V. I.; Lisitsyna, L. A.; Andryuschenko, L. A.; Yakubovskaya, A. G.; Vovk, O. M.; *J. Lumin.* **2014**, *153*, 130. [Crossref]

8. Ribeiro, R. A. P.; Oliveira, M. C.; Bomio, M. R. D.; de Lazaro, S. R.; Andrés, J.; Longo, E.; *Appl. Surf. Sci.* **2020**, *509*, 145321. [Crossref]

9. Kumar, M.; Lamba, V. K.; *AIP Conf. Proc.* **2019**, *2142*, 140033. [Crossref]

10. Mimouni, R.; Boubaker, K.; Amlouk, M.; *J. Alloys Compd.* **2015**, *624*, 189. [Crossref]

11. Pan, L.; Li, L.; Chen, Y.; *J. Sol-Gel Sci. Technol.* **2013**, *66*, 330. [Crossref]

12. Ramezani, M.; Pourmortazavi, S. M.; Sadeghpur, M.; Yazdani, A.; Kohsari, I.; *J. Mater. Sci.: Mater. Electron.* **2015**, *26*, 3861. [Crossref]

13. Wang, B.-Y.; Zhang, G.-Y.; Cui, G.-W.; Xu, Y.-Y.; Liu, Y.; Xing, C.-Y.; *Inorg. Chem. Front.* **2019**, *6*, 209. [Crossref]

14. Cavalcante, L. S.; Almeida, M. A. P.; Avansi Jr., W.; Tranquilin, R. L.; Longo, E.; Batista, N. C.; Mastelaro, V. R.; Li, M. S.; *Inorg. Chem.* **2012**, *51*, 10675. [Crossref]

15. Roca, R. A.; Sczancoski, J. C.; Nogueira, I. C.; Fabbro, M. T.; Alves, H. C.; Gracia, L.; Santos, L. P. S.; de Sousa, C. P.; Andrés, J.; Luz Jr., G. E.; Longo, E.; Cavalcante, L. S.; *Catal. Sci. Technol.* **2015**, *5*, 4091. [Crossref]

16. Singh, J.; Kumari, P.; Basu, S.; *J. Photochem. Photobiol., A* **2019**, *371*, 136. [Crossref]

17. de Foggi, C. C.; de Oliveira, R. C.; Fabbro, M. T.; Vergani, C. E.; Andres, J.; Longo, E.; Machado, A. L.; *Cryst. Growth Des.* **2017**, *17*, 6239. [Crossref]

18. Foggi, C. C.; Fabbro, M. T.; Santos, L. P. S.; de Santana, Y. V. B.; Vergani, C. E.; Machado, A. L.; Cordoncillo, E.; Andrés, J.; Longo, E.; *Chem. Phys. Lett.* **2017**, *674*, 125. [Crossref]

19. Liu, D.; Huang, W.; Li, L.; Liu, L.; Sun, X.; Liu, B.; Yang, B.; Guo, C.; *Nanotechnology* **2017**, *28*, 385702. [Crossref]

20. Silva, M. D. P.; Gonçalves, R. F.; Nogueira, I. C.; Longo, V. M.; Mondoni, L.; Moron, M. G.; Santana, Y. V.; Longo, E.; *Spectrochim. Acta, Part A* **2016**, *153*, 428. [Crossref]

21. San-Miguel, M. A.; da Silva, E. Z.; Zanetti, S. M.; Cilense, M.; Fabbro, M. T.; Gracia, L.; Andrés, J.; Longo, E.; *Nanotechnology* **2016**, *27*, 225703. [Crossref]

22. Macedo, N. G.; Gouveia, A. F.; Roca, R. A.; Assis, M.; Gracia, L.; Andrés, J.; Leite, E. R.; Longo, E.; *J. Phys. Chem. C* **2018**, *122*, 8667. [Crossref]

23. Singh Bakshi, M.; *Cryst. Growth Des.* **2016**, *16*, 1104. [Crossref]

24. Kokilavani, S.; Syed, A.; Raaja Rajeshwari, M.; Subhiksha, V.; Elgorban, A. M.; Bahkali, A. H.; Zaghloul, N. S. S.; Das, A.; Sudheer Khan, S.; *J. Alloys Compd.* **2022**, *889*, 161662. [Crossref]

25. de Foggi, C. C.; de Oliveira, R. C.; Assis, M.; Fabbro, M. T.; Mastelaro, V. R.; Vergani, C. E.; Gracia, L.; Andrés, J.; Longo, E.; Machado, A. L.; *Mater. Sci. Eng. C* **2020**, *111*, 110765. [Crossref]

26. Andrade Neto, N. F.; Oliveira, P. M.; Bomio, M. R. D.; Motta, F. V.; *Ceram. Int.* **2019**, *45*, 15205. [Crossref]

27. Silva, F. C. M.; Silva, L. K. R.; Santos, A. G. D.; Caldeira, V. P. S.; Cruz-Filho, J. F.; Cavalcante, L. S.; Longo, E.; Luz Jr., E. S.; *J. Inorg. Organomet. Polym. Mater.* **2020**, *30*, 3626. [Crossref]

28. Gusmão, S. B. S.; Ghosh, A.; Marques, T. M. F.; Gusmão, G. O. M.; Oliveira, T. G.; Cavalcante, L. C. D.; Vasconcelos, T. L.; Abreu, G. J. P.; Guerra, Y.; Peña-Garcia, R.; Santos, F. E. P.; Viana, B. C.; *J. Phys. Chem. Solids* **2020**, *145*, 109561. [Crossref]

29. Herron, S. M.; Tanskanen, J. T.; Roelofs, K. E.; Bent, S. F.; *Chem. Mater.* **2014**, *26*, 7106. [Crossref]

30. Nobre, F. X.; Bastos, I. S.; Fontenelle, R. O. S.; Araújo Jr., E. A.; Takeno, M. L.; Manzato, L.; de Matos, J. M. E.; Orlandi, P. P.; Mendes, J. F. S.; Brito, W. R.; Couceiro, P. R. C.; *Ultrason. Sonochem.* **2019**, *58*, 104620. [Crossref]

31. Longo, E.; Volanti, D. P.; Longo, V. M.; Gracia, L.; Nogueira, I. C.; Almeida, M. A. P.; Pinheiro, A. N.; Ferrer, M. M.; Cavalcante, L. S.; Andrés, J.; *J. Phys. Chem. C* **2014**, *118*, 1229. [Crossref]

32. Zhang, J.; Yan, X.; Hu, X.; Feng, R.; Zhou, M.; *Chem. Eng. J.* **2018**, *347*, 640. [Crossref]

33. Chen, J.; Zhao, W.; Wu, Q.; Mi, J.; Wang, X.; Ma, L.; Jiang, L.; Au, C.; Li, J.; *Chem. Eng. J.* **2020**, *382*, 122910. [Crossref]

34. Bai, S.; Wang, L.; Li, Z.; Xiong, Y.; *Adv. Sci.* **2017**, *4*, 1600216. [Crossref]

35. Pereira, W. D. S.; Ferrer, M. M.; Botelho, G.; Gracia, L.; Nogueira, I. C.; Pinatti, I. M.; Rosa, I. L. V.; La Porta, F. D. A.; Andrés, J.; Longo, E.; *Phys. Chem. Chem. Phys.* **2016**, *18*, 21966. [Crossref]

36. Andrés, J.; Gracia, L.; Gonzalez-Navarrete, P.; Longo, V. M.; Avansi, W.; Volanti, D. P.; Ferrer, M. M.; Lemos, P. S.; La Porta, F. A.; Hernandes, A. C.; Longo, E.; *Sci. Rep.* **2014**, *4*, 5391. [Crossref]

37. Longo, E.; Avansi, W.; Bettini, J.; Andrés, J.; Gracia, L.; *Sci. Rep.* **2016**, *6*, 21498. [Crossref]

38. Mondego, M.; de Oliveira, R. C.; Penha, M.; Li, M. S.; Longo, E.; *Ceram. Int.* **2017**, *43*, 5759. [Crossref]

39. Zhang, X.-Y.; Wang, J. D.; Liu, J. K.; Yang, X.-H.; Lu, Y.; *CrystEngComm* **2015**, *17*, 1129. [Crossref]

40. Wang, F.; Wang, X.; Chang, Z.; Zhu, Y.; Fu, L.; Liu, X.; Wu, Y.; *Nanoscale Horiz.* **2016**, *1*, 272. [Crossref]

41. Mayerhöfer, T.; *Vib. Spectrosc.* **2004**, *35*, 67. [Crossref]

42. Longo, V. M.; De Foggi, C. C.; Ferrer, M. M.; Gouveia, A. F.; André, R. S.; Avansi, W.; Vergani, C. E.; Machado, A. L.; Andrés, J.; Cavalcante, L. S.; Hernandes, A. C.; Longo, E.; *J. Phys. Chem. A* **2014**, *118*, 5769. [Crossref]

43. Selvamani, M.; Krishnamoorthy, G.; Ramadoss, M.; Sivakumar, P. K.; Settu, M.; Ranganathan, S.; Vengidusamy, N.; *Mater. Sci. Eng., C* **2016**, *60*, 109. [Crossref]

44. Gouveia, A. F.; Sczancoski, J. C.; Ferrer, M. M.; Lima, A. S.; Santos, M. R. M. C.; Li, M. S.; Santos, R. S.; Longo, E.; Cavalcante, L. S.; *Inorg. Chem.* **2014**, *53*, 5589. [Crossref]

45. George, T.; Joseph, S.; Mathew, S.; *J. Phys.* **2005**, *65*, 793. [Crossref]

46. Pinatti, I. M.; Nogueira, I. C.; Pereira, W. S.; Pereira, P. F. S.; Gonçalves, R. F.; Varela, J. A.; Longo, E.; Rosa, I. L. V.; *Dalton Trans.* **2015**, *44*, 17673. [Crossref]

47. Pinatti, I. M.; Ireland, T. G.; Fern, G. R.; Rosa, I. L. V.; Silver, J.; *J. Mater. Sci.: Mater. Electron.* **2017**, *28*, 7029. [Crossref]

48. Ayappan, C.; Palanivel, B.; Jayaraman, V.; Maiyalagan, T.; Mani, A.; *Mater. Sci. Semicond. Process.* **2019**, *104*, 104693. [Crossref]

49. Pereira, P. F. S.; Santos, C. C.; Gouveia, A. F.; Ferrer, M. M.; Pinatti, I. M.; Botelho, G.; Sambrano, J. R.; Rosa, I. L. V.; Andrés, J.; Longo, E.; *Inorg. Chem.* **2017**, *56*, 7360. [Crossref]

50. *ImageJ*, version 1.8.0; U. S. National Institutes of Health, Bethesda, Maryland, USA, 2015.

51. Miranda, M. A. R.; Sasaki, J. M.; *Acta Cryst.* **2018**, *A74*, 54. [Crossref]

52. Londoño-Restrepo, S. M.; Jeronimo-Cruz, R.; Millán-Malo, B. M.; Rivera-Muñoz, E. M.; Rodriguez-García, M. E.; *Sci. Rep.* **2019**, *9*, 5915. [Crossref]

53. Piga, G.; Malgosa, A.; Thompson, T. J. U.; Enzo, S.; *J. Archaeol. Sci.* **2008**, *35*, 2171. [Crossref]

54. Bastús, N. G.; Merkoçi, F.; Piella, J.; Puntes, V.; *Chem. Mater.* **2014**, *26*, 2836. [Crossref]

55. Pillai, Z. S.; Kamat, P. V.; *J. Phys. Chem. B* **2004**, *108*, 945. [Crossref]

56. Park, J.; Joo, J.; Soon, G. K.; Jang, Y.; Hyeon, T.; *Angew. Chem., Int. Ed.* **2007**, *46*, 4630. [Crossref]

57. Jin, B.; Liu, Z.; Tang, R.; *CrystEngComm* **2020**, *22*, 4057. [Crossref]

58. Polte, J.; *CrystEngComm* **2015**, *17*, 6809. [Crossref]

59. Thanh, N. T. K.; Maclean, N.; Mahiddine, S.; *Chem. Rev.* **2014**, *114*, 7610. [Crossref]

60. de Santana, Y. V. B.; Gomes, J. E. C.; Matos, L.; Cruvinel, G. H.; Perrin, A.; Perrin, C.; Andrès, J.; Varela, J. A.; Longo, E.; *Nanomater. Nanotechnol.* **2014**, *4*, 1. [Crossref]

61. *KrystalShaper software*, version 1.3.1; JCrystalSoft, 2006-2022.

62. Tang, J.; Ye, J.; *J. Mater. Chem.* **2005**, *15*, 4246. [Crossref]

63. Chen, H.; Xu, Y.; *Appl. Surf. Sci.* **2014**, *319*, 319. [Crossref]

Submitted: August 18, 2022

Published online: January 20, 2023